WRF modeling of PM$_{2.5}$ remediation by SALSCS and its clean air flow over Beijing terrain

Qingfeng Cao, Lian Shen, Sheng-Chieh Chen, David Y.H. Pui *

Department of Mechanical Engineering, University of Minnesota, 111 Church Street SE, Minneapolis, MN 55455, USA

HIGHLIGHTS

- SALSCS is a large-scale cleaning system proposed for urban air pollution reduction.
- WRF simulations were conducted to evaluate SALSCS over the Beijing terrain.
- Passive tracer scalars were used to simulate PM$_{2.5}$ pollutant and SALSCS clean air.
- Air pollution reduction percentages of SALSCS over the urban region were obtained.
- Clean air plumes of SALSCS were visualized.

GRAPHICAL ABSTRACT
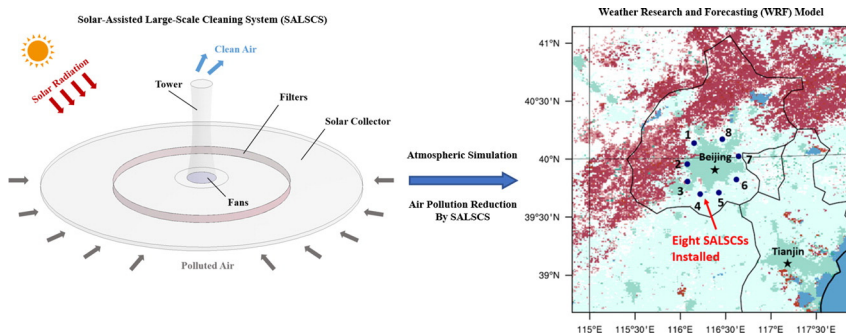
ABSTRACT

Atmospheric simulations were carried out over the terrain of entire Beijing, China, to investigate the effectiveness of an air-pollution cleaning system named Solar-Assisted Large-Scale Cleaning System (SALSCS) for PM$_{2.5}$ mitigation by using the Weather Research and Forecasting (WRF) model. SALSCS was proposed to utilize solar energy to generate airflow therefrom the airborne particulate pollution of atmosphere was separated by filtration elements. Our model used a derived tendency term in the potential temperature equation to simulate the buoyancy effect of SALSCS created with solar radiation on its nearby atmosphere. PM$_{2.5}$ pollutant and SALSCS clean air were simulated in the model domain by passive tracer scalars. Simulation conditions with two system flow rates of 2.64×10^5 m^3/s and 3.80×10^5 m^3/s were tested for seven air pollution episodes of Beijing during the winters of 2015–2017. The numerical results showed that with eight SALSCSs installed along the 6th Ring Road of the city, 11.2% and 14.6% of PM$_{2.5}$ concentrations were reduced under the two flow-rate simulation conditions, respectively.

© 2018 Elsevier B.V. All rights reserved.

1. Introduction

Many urban areas in the world are currently experiencing severe air pollution problems, adversely affecting the health and living quality of the city population (Seaton et al., 1995; Kampa and Castanas, 2008; Shah et al., 2013; Chen Y. et al., 2013). For instance, Beijing, the capital city of China, has been facing high concentrations of PM$_{2.5}$ (fine particulate matter <2.5 μm) and gaseous pollutions over the last two decades (Tang et al., 2017; Zhang et al., 2016; Sun et al., 2016; Hao et al., 2007). Most of the strategies for air pollution mitigation are targeted on cutting the pollutant emissions from the sources (Pui et al., 2014; Wang et al., 2016a; Wang et al., 2016b; Shi et al., 2016; Mao et al., 2014; Wang et al., 2017), but not reducing the air pollutions after their emission and dispersion into the atmosphere. Recently, a Solar-Assisted Large-Scale Cleaning System (SALSCS) was proposed by Cao et al. (2015) as a

* Corresponding author.
  E-mail address: dyhpui@umn.edu (D.Y.H. Pui).

novel strategy aimed at generating airflow in large quantities to facilitate the separation of $PM_{2.5}$ from polluted atmospheric air for urban areas.

The idea of SALSCS utilizing solar energy to generate updraft airflow originated from the configuration of solar chimney power plant first described by a Spanish artillery colonel, Isidoro Cabanyes, in 1903 (Al-Kayiem and Aja, 2016; Kasaeian et al., 2017). The system was proven to work after a pilot plant was constructed and tested in Manzanares, Spain (Haaf et al., 1983; Haaf, 1984). Many seminal works have been done over the last 30 years, demonstrating the system's capability of creating airflow (Pasumarthi and Sherif, 1998a; Pasumarthi and Sherif, 1998b; Pastohr et al., 2004; Schlaich et al., 2005; Pretorius and Kröger, 2006; Ming et al., 2008; Fasel et al., 2013). A schematic configuration was presented as an initial design of a full-scale system as shown in Fig. 1. The SALSCS is composed of four basic elements: (1) a solar collector, (2) a tower, (3) filtration elements and (4) fans for creating more airflow if necessary. The system generates updraft airflow based on the principle of buoyancy effect with solar energy. After heated by the sunlight, the warmer air inside the system has a lower density than the air in the ambient environment, so that buoyancy-driven flow is induced. Fans can also be employed to generate higher flow rate. Atmospheric polluted air is pulled into the system at the solar collector aperture, flows over the warm ground heated by solar radiation under the collector shed, and passes through the filtration elements for the removal of $PM_{2.5}$. It is to be mentioned that, in addition to $PM_{2.5}$, gaseous pollutants can also be mitigated if selected chemical filters are applied. However, $PM_{2.5}$ is the concerned air pollutant in this study. The filtered and cleaned air with low $PM_{2.5}$ concentration then enters the tower and is delivered back into the atmosphere.

Cao et al. (2015) conducted a numerical calculation and estimated the total flow rate of the full-scale SALSCS to be 2.64×10^5 m^3/s with a filter bank installed in the system, where Reynolds-Averaged Navier-Stokes (RANS) equations were solved together with the standard k-ε 2-equation turbulent model using the ANSYS Fluent software. As a validation of the calculated system flow rate, a demonstration unit of SALSCS was constructed in the city of Xi'an, China, during the summer of 2016. Experimental measurements were conducted to evaluate the system performance. The obtained measurement data showed a good agreement with the numerical results calculated from the same ANSYS Fluent solver. Comparisons between the experimental data and numerical results are given in the Supporting Information of this paper, and detailed descriptions of this validation study will be published in the near future.

Given the high flow rate of SALSCS according to the calculation of Cao et al. (2015), it is interesting to find out how much of air quality can be improved over urban areas by implementing an array of SALSCSs. Thus, atmospheric simulations at meteorological scale over the terrain of certain urban areas were conducted. A computer program named

Fig. 1. Schematic diagram of the SALSCS with (1) solar collector, (2) tower, (3) filtration elements, and (4) fans (optional).

Weather Research and Forecasting (WRF) model was utilized for the purpose of this study.

WRF is a meteorological numerical simulation program designed for both operational weather forecasting and atmospheric research (http://www.wrf-model.org). The model can be used to simulate atmospheric processes over varied ranges of spatial and temporal scales (Skamarock et al., 2008). Many researchers employed the WRF program to study the processes of air pollution emission, generation and transportation in the atmosphere. For example, Ahmadov et al. (2015) modeled the wintertime ozone over the Unita Basin in northeastern Utah, USA, to examine the different factors for ozone formation. The study showed that there was a disproportionate contribution of aromatic VOCs to ozone formation relative to the other VOC emissions. Beck et al. (2013) carried out atmospheric simulations using WRF to study the ration of CH_4 mixing over the Amazon basin in South America. The major conclusions were that a wetland inundation map with inundated area as a function of time can improve the agreement with the observations, and improvements in representing the meteorological conditions are necessary for modeling accuracy. Chen D. et al. (2013) used WRF to simulate the effects of O_3 and NO_x species and their photochemistry on air quality in the Los Angeles basin. Results indicated NO_x-saturated O_3 production in the basin as a result of the O_3 concentration increase with modifying the NO_x emission reduction of the model. The WRF program was applied by Matsui et al. (2010) to study how individual aerosol chemical components affect the spatial and temporal variations of aerosol optical properties in the region of Beijing, China. It was found that aerosol optical parameters are related to synoptic meteorological conditions and spatial variations of elemental carbon and sulfate. Jiang et al. (2008) applied WRF simulations to study a continuous photochemical pollution episode in Hong Kong during Typhoon Nari, with the aim to understand the physical and chemical mechanisms of the air pollution episode. The authors concluded that meteorological conditions, such as high temperature, low relative humidity and stable boundary layer structure, provide major contributions to the pollution formation and maintenance. Although there are many researchers conducting atmospheric simulations to study different air pollution mechanisms, no research has been done so far to study the influence of a large-scale air pollution control system, e.g. the current SALSCS, on $PM_{2.5}$ remediation over urban regions. Because of the capability of WRF, we chose to use its modeling system to carry out atmospheric simulations to investigate the effectiveness of SALSCS on reducing urban $PM_{2.5}$. Most of the research mentioned above utilized the WRF-Chem model to simulate air pollution episodes, which is a version of WRF that can simulate trace gases and particulates simultaneously within the meteorological fields (Grell et al., 2005). Since our main focus is only on the physical transport process of the air pollution in the atmosphere and the physical mechanism of SALSCS collecting $PM_{2.5}$ and delivering clean air, chemical processes were neglected in our simulation. Hence, we employed the WRF model to carry out atmospheric simulations as an initial study of evaluating the effectiveness of SALSCS on urban air pollution remediation.

Beijing is a megacity rapidly developing in the northern China and experiences severe air pollution problems during the recent decades. Thus, our WRF simulation was chosen to be carried out over the terrain of the Beijing city and its surrounding regions. The present study is aimed to determine the air-pollution reduction by SALSCS over the city, and the amount of clean air reaching the ground level of its urban area. This paper first discusses the WRF model formulation, including the setup for the model domain and selection of the physics parameterization schemes. Then the approach of modeling the buoyancy effect created by SASLCS in the WRF model is introduced. The method for simulating $PM_{2.5}$ pollutant and SALSCS clean air is then addressed in the following sections. Numerical results on both the air pollution and clean air are presented and analyzed in the Results and discussion section. At the end of this paper, a summary of the current research work is given and possible future work is discussed.
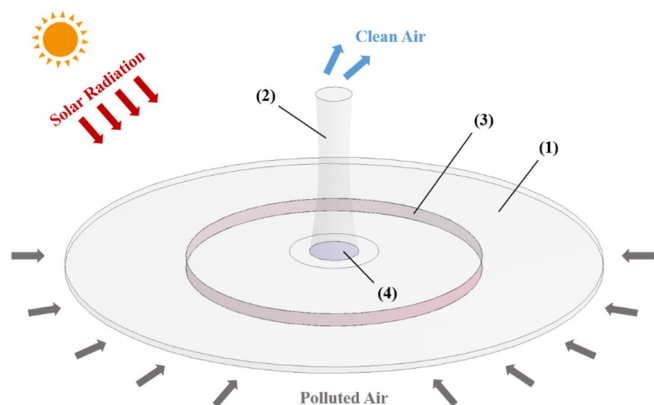
2. Configuration of the WRF model

The WRF model solves the three-dimensional inviscid Euler equations using a terrain-following hydrostatic pressure vertical coordinate for the flow field in the simulation domain. It is fully compressible so that high-frequency acoustic and gravity waves in the atmosphere can be simulated. A non-hydrostatic version of the model was selected for our case in order to simulate small-scale atmospheric flows with length scales in the order of a few kilometers or less where the vertical motion in the atmosphere cannot be neglected. All the governing equations are cast into a conserving flux form, which can be referred to the technical note of WRF by Skamarock et al. (2008).

There are three nested computational domains employed in our model defined on a Mercator projection. The outer and medium domains have a horizontal grid dimension of 15 km and 3 km, respectively. Fig. 2 shows the inner domain with Beijing located at the domain center, where the topography data of the area is presented as well. In the lower right corner is the city of Tianjin, which is another major city of the region. This inner domain extends from 38.6° N to 41.2° N (267 grid points) in the north-south direction and from 114.8° E to 118.4° E (267 grid points) in the east-west direction at a horizontal grid spacing of 1×1 km^2. The vertical grid is composed of 45 levels from the ground surface to the height with a constant pressure of 5000 Pa (~20 km). The static geographical fields, such as terrain height, soil properties and land use, etc., were interpolated onto our model domain by using the WRF preprocessing system (WPS) from the MODIS data with a resolution of 30 seconds (~1 km). The computational domain encompasses a widely varying landscape with highly elevated mountains (>2500 m) in the north and west directions of the Beijing city and low altitude plains (<500 m) in the south and east directions. The data for driving the initial and boundary conditions for the meteorological fields was interpolated from the National Center for Environmental Prediction (NCEP) Final Analysis (FNL) data available every 6 h at a horizontal spatial resolution of 0.25-degree by 0.25-degree (~27 × 27 km^2). The WRF model applies the Arakawa C-grid as its grid staggering, where velocities are staggered half grid dimension from the scalar variables

(Skamarock et al., 2008; Arakawa and Lamb, 1977). A Runge-Kutta third-order time integration scheme (RK3) is employed with a time-splitting integration method applied to integrate the fully-compressible Euler equations. A fully-compressible atmospheric model includes high-frequency modes (acoustic and gravity waves) in the simulation, which are meteorologically insignificant motions. Much smaller time step size of the RK3 scheme should be applied to simulate the high-frequency modes. The time-splitting method in WRF allows the model to calculate the high-frequency modes with a smaller time step size during each sub-step of RK3 integration, and calculate the meteorological-significant low-frequency modes with a larger RK3 time step size to save computational time (Skamarock and Klemp, 2008; Wicker and Skamarock, 2002). The time step size of the RK3 integration for our inner domain was chosen to be 6 s. An overview of the physics scheme options applied for our simulations is given in Table 1.

3. SASLCS in WRF model

In this section, we introduce the method for simulating the effect of buoyancy generated by SALSCS on its surrounding atmosphere in the WRF model. The solar collector of a full-scale system occupies a large area. Thus, it should be built in suburb regions next to the city where enough lands are available for system construction. In our model, there are in total eight SALSCSs installed in the surrounding areas of the Beijing city as shown in Fig. 3, where the land use category data of the inner model domain is presented. The color marked with No. 13 indicates the urban regions. The two major metropolitan areas of Beijing and Tianjin within the model domain are clearly displayed in the figure with the two black stars to locate the downtown areas of the two cities, respectively. The total urban area of Beijing is estimated to be about 1400 km^2. The eight blue points present the locations of the eight SALSCSs in the WRF model, illustrating that the systems are installed in the suburb regions next to the 6th Ring Road of the city. Table 2 gives the longitudes and latitudes for all the eight full-scale SALSCSs installed in the WRF model domain.

Since SALSCS utilizes the buoyancy principle to generate updraft airflow, an extra temperature tendency term was added to the energy equation of the WRF model at each location of the eight SALSCSs to simulate their effects on the nearby atmospheric dynamics. By including the temperature tendency term to the energy equation, it is like heating the air at the SALSCS location with a heat flux corresponding to the solar radiation received by the solar collector. Given that WRF is a fully-compressible model, the applied heat flux causes the warmer air at a
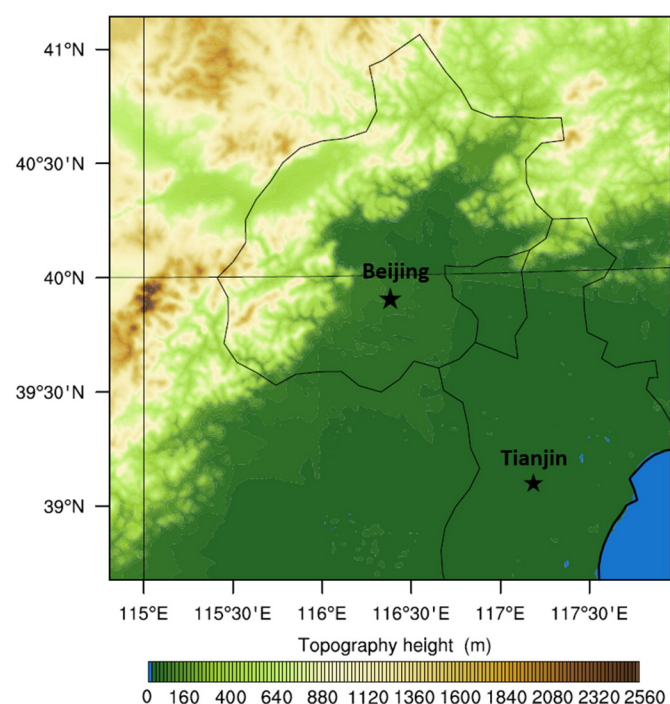

Fig. 2. The WRF inner domain showing topography with the locations of Beijing and Tianjin highlighted.

Table 1
Physics parameterization schemes employed by the WRF model.

| Atmospheric process	Physics parameterization schemes
Microphysics	WSM 6-class graupel scheme
	Hong and Lim (2006)
Long-wave radiation	Rapid Radiative Transfer Model (RRTM)
	Mlawer et al. (1997)
Short-wave radiation	Dudhia scheme
	Dudhia (1989)
Surface layer	Revised MM5 Monin-Obukhov scheme
	Jiménez et al. (2012)
Land-surface model	Unified Noah land-surface model
	Chen and Dudhia (2001a, 2001b); Ek et al. (2003)
Planetary boundary layer	YSU scheme
	Hong et al. (2006)
Cumulus parameterization (for the outer domain only)	Grell-Freitas scheme
	Grell and Freitas (2013)
Urban Surface	Urban canopy model
	Kusaka et al. (2001); Kusaka and Kimura (2004)
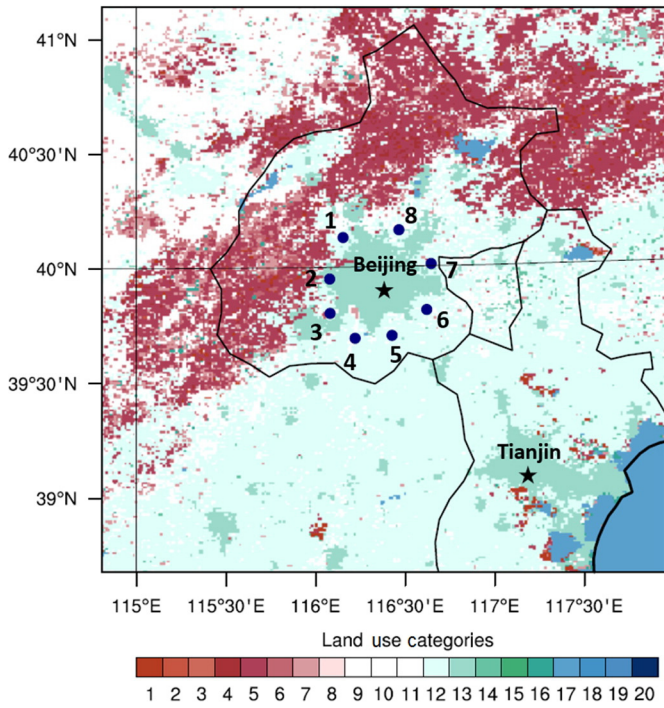
Fig. 3. Land use categories over the computational domain with the blue points displaying locations of the eight SALSCSs installed next to the 6th Ring Road of the Beijing city. Land use categories displayed in the figure: 1. evergreen needleleaf forest; 2. evergreen broadleaf forest; 3. deciduous needleleaf forests; 4. deciduous broadleaf forests; 5. mixed forests; 6. closed shrublands; 7. open shrublands; 8. woody savannas; 9. savannas; 10. grasslands; 11. permanent wetlands; 12. croplands; 13. urban and built-up; 14. cropland/natural vegetation mosaic; 15. snow and ice; 16. barren or sparsely vegetated; 17. water; 18. wooded tundra; 19. mixed tundra; 20. barren tundra.

SASLCS location to have a lower density. Thus, the buoyancy-driven effect of SALSCS is included in the model. A brief derivation of the temperature tendency term is given as follows.

The original thermal energy equation for dry air of a compressible and inviscid flow is written as

$$\frac{\partial T}{\partial t} + u\frac{\partial T}{\partial x} + v\frac{\partial T}{\partial y} + w\frac{\partial T}{\partial z} = -\frac{RT}{c_v}\left(\frac{\partial u}{\partial x} + \frac{\partial v}{\partial y} + \frac{\partial w}{\partial z}\right) + \frac{Q}{c_v}, \qquad (1)$$

which is referred to Laprise (1992) and Kundu et al. (2011). Here, T is the temperature, and u, v, and w are the three velocity components in the x, y, and z directions, respectively. c_v is the specific heat at constant volume, R is the specific gas constant of dry air, and Q is the solar heating rate per unit dry air mass with the units of J/kg-s.

Table 2
Longitudes and latitudes of the eight SASLCSs in the WRF model.

SALSCS no.	Longitude	Latitude
1	116.18° E	40.13° N
2	116.10° E	39.95° N
3	116.10° E	39.80° N
4	116.24° E	39.69° N
5	116.45° E	39.70° N
6	116.65° E	39.81° N
7	116.68° E	40.01° N
8	116.50° E	40.16° N

The flux-form potential temperature equation solved in the WRF model is given by Skamarock et al. (2008) with the mapping factors ignored and Cartesian coordinate applied in the vertical direction,

$$\frac{\partial(\mu_d\theta)}{\partial t} + \frac{\partial(\mu_d u\theta)}{\partial x} + \frac{\partial(\mu_d v\theta)}{\partial y} + \frac{\partial(\mu_d w\theta)}{\partial z} = \mu_d F, \qquad (2)$$

where $\mu_d \equiv p_{dhs} - p_{dht}$, representing the mass per unit area of a column in the WRF model domain. p_{dh} is the hydrostatic pressure of the dry atmosphere, and p_{dhs} and p_{dht} are the hydrostatic pressure at the bottom and top of the simulated atmosphere, respectively. θ is the potential temperature defined as

$$\theta \equiv T(p_0/p)^{R/c_p}, \qquad (3)$$

where c_p is the specific heat at constant pressure, and p_0 is a reference pressure of 10^5 Pa. The term on the right-hand side of Eq. (2) is the temperature tendency term that we seek to apply at the SALSCS locations.

To find an expression for F, we first re-write Eq. (2) in the primitive form as

$$\frac{\partial \theta}{\partial t} + u\frac{\partial \theta}{\partial x} + v\frac{\partial \theta}{\partial y} + w\frac{\partial \theta}{\partial z} = F, \qquad (4)$$

and then need to translate Eqs. (4) into (1). After substituting Eqs. (3) into (4), we obtain the following equation as

$$\frac{DT}{Dt} - \frac{RT}{c_p}\frac{1}{p}\frac{Dp}{Dt} = F \cdot \left(p_0^{-R/c_p} p^{R/c_p}\right), \qquad (5)$$

with

$$\frac{D}{Dt} = \frac{\partial}{\partial t} + u\frac{\partial}{\partial x} + v\frac{\partial}{\partial y} + w\frac{\partial}{\partial z} \qquad (6)$$

as the material derivative of a variable. An ideal gas follows the equation of state as

$$p = \rho RT. \qquad (7)$$

By substituting Eq. (7) into the second term on the left-hand side of Eq. (5), we obtain the following equation,

$$\left(\frac{c_p - R}{c_p}\right)\frac{DT}{Dt} - \frac{RT}{\rho c_p}\frac{D\rho}{Dt} = F \cdot \left(p_0^{-R/c_p} p^{R/c_p}\right). \qquad (8)$$

The laws of thermodynamics give the relation between c_p and c_v for an ideal gas as

$$c_p - c_v = R. \qquad (9)$$

By applying the above relation, Eq. (8) is re-written as

$$\frac{DT}{Dt} - \frac{RT}{\rho c_v}\frac{D\rho}{Dt} = \frac{c_p}{c_v} F \cdot \left(p_0^{-R/c_p} p^{R/c_p}\right). \qquad (10)$$

And by substituting the continuity equation for a compressible flow,

$$\frac{D\rho}{Dt} + \rho\left(\frac{\partial u}{\partial x} + \frac{\partial v}{\partial y} + \frac{\partial w}{\partial z}\right) = 0, \qquad (11)$$

into Eq. (10), we obtain the following equation for temperature

$$\frac{DT}{Dt} = -\frac{RT}{c_v}\left(\frac{\partial u}{\partial x} + \frac{\partial v}{\partial y} + \frac{\partial w}{\partial z}\right) + \frac{c_p}{c_v} F \cdot \left(p_0^{-R/c_p} p^{R/c_p}\right). \qquad (12)$$

Eq. (12) derived from Eq. (2), the potential temperature equation solved in the WRF model, has the same form as Eq. (1), the original thermal energy equation for a compressible and inviscid flow. By equating

the source terms of Eqs. (1) and (12), we find the expression for F in the potential temperature tendency term of Eq. (2) as

$$F = \frac{Q}{c_p} p_0^{R/c_p} p^{-R/c_p}. \tag{13}$$

As mentioned previously, Q is the solar heating rate per unit dry air mass received by SALSCS. If the total area of the SASLCS solar collector is A, the solar heat flux is q (W/m^2), and this amount of solar energy is assumed to be applied to the one column of grid cells representing the system tower of SASLCS in the WRF model with a total dry air mass of m_d, then the solar heating rate can be expressed as

$$Q = qA/m_d. \tag{14}$$

Our current WRF model has a grid spacing of 1×1 km^2 in the horizontal directions, so the SALSCS geometry cannot be fully resolved in the simulation. As a simplification, the solar collector of SALSCS is represented by nine grid cells at the lowest model level so that it has a square geometry with a side length of 3 km, and the system tower is one column of grid cells in the middle of the solar collector with a height of about 120 m, which is different from the original full-scale SALSCS proposed by Cao et al. (2015) with a circular solar collector of 2.5 km in radius and a tower height of 500 m. As we have tested in the WRF model, if the SALSCS clean air is released from a lower tower, it is easier to reach the ground level in the urban area of Beijing. The difference in system flow rate due to changes in the dimension of solar collector and tower height can be compensated by the utilization of fans so that the SALSCS in the current WRF model was assumed to generate the same flow rate as the originally proposed full-scale system. According to the calculation of Cao et al. (2015), the full-scale SASLCS generates a flow rate of 3.80×10^5 m^3/s with a solar heat flux of 640 W/m^2 before the installation of the filter bank, and the flow rate reduces to 2.64×10^5 m^3/s after the pressure drop of the filter bank is considered. In this study, we assumed that the system flow rate is linearly proportional to the solar heat flux. Therefore, with a solar heat flux, q, of 640 W/m^2 corresponding to a flow rate of 3.80×10^5 m^3/s, the solar heat flux related to a flow rate of 2.64×10^5 m^3/s is calculated as 445 W/m^2. Both the system flow rates were applied in the current WRF model to determine how much the full-scale SALSCS is able to reduce the air pollution over the urban areas of Beijing.

4. Method of creating PM$_{2.5}$ field

PM$_{2.5}$ pollutant over the terrain of Beijing was simulated by a passive tracer scalar to understand the effectiveness of the eight SALSCSs on the air pollution reduction of the city. As indicated by Skamarock et al. (2008), passive tracer scalar in WRF is defined as the mass mixing ratio of the scalar to the dry air (mass per mass of dry air), which has no influence on the computational fields, but only follows the movement of atmospheric flows. In WRF model, the dry air mass of a grid cell is expressed as

$$m_d = \Delta\eta(\Delta x/f_x)\left(\Delta y/f_y\right)(\mu_d/g), \tag{15}$$

where $\Delta\eta$ is the vertical grid spacing of the grid cell, and η denotes the model vertical coordinate defined as

$$\eta = \frac{p_{dh} - p_{dht}}{\mu_d}. \tag{16}$$

Δx and Δy in Eq. (15) are the grid spacings in the two horizontal directions, respectively, and f_x and f_y are the corresponding mapping factors, which translate the grid distance to the real distance on earth's surface and is defined as the ratio of the two. g is the gravitational acceleration. The mass of air pollutant in a grid cell is then calculated as $\phi_p m_d$,

where ϕ_p is the local value of the tracer scalar indicating the mass mixing ratio of the air pollutant. In this study, we assumed that the air pollutant added into our WRF model is PM$_{2.5}$ only. The total PM$_{2.5}$ mass is calculated as the sum of $\phi_p m_d$ at each grid cell over the entire computational domain.

To include the passive tracer scalar of the PM$_{2.5}$ pollutant, we first need to estimate the emission rate of PM$_{2.5}$ in the Beijing city. The U.S. embassy of China in Beijing measures the local real-time PM$_{2.5}$ concentration every day, and the historical hourly data are available on the website of http://www.stateair.net since the year of 2008, giving attribution to the U.S. Department of State. Although as indicated by their website, the data are not fully verified or validated, they can help researchers estimate the emission rates of PM$_{2.5}$ in the city of Beijing. Fig. 4 shows the downloaded real-time PM$_{2.5}$ concentration data in 72 h during seven air pollution episodes of the city in the winters of 2015–2017, where each episode is represented by a colored curve with different symbols. The figure legend indicates the local starting and ending times of each episode. A time filter of 1 h was applied to calculate the average emission rates for each case based on the PM$_{2.5}$ concentration data shown in the figure. If a curve has a positive gradient during a time filter, it is considered as the average concentration growth rate or emission rate of PM$_{2.5}$ during that 1 h. By taking the average value of the positive filtered gradients for each curve during the 72-hour pollution period, we obtained the average PM$_{2.5}$ emission rates of the Beijing city for the seven air pollution episodes. The calculated results are listed in Table 3.

The obtained PM$_{2.5}$ emission rates of the Beijing city were applied to include PM$_{2.5}$ pollutant into the WRF model domain to generate a pollutant field for our study. We should also find the formula describing the pollution emission process during each time step, Δt, of the RK3 integration. The PM$_{2.5}$ concentration at a grid cell location, C_p, is expressed by the following equation,

$$C_p = \frac{\phi_p m_d}{V_g} = \phi_p \rho_d, \tag{17}$$

where V_g is the volume of the grid cell and ρ_d is the density of the dry air inside the grid volume. The concentration increase caused by air pollution emission during a model time step is then calculated as

$$\Delta C_p = \phi_{p2}\rho_{d2} - \phi_{p1}\rho_{d1}, \tag{18}$$

where the subscripts 1 and 2 indicate model properties before and after the emission, respectively. With the calculated PM$_{2.5}$ pollutant emission rate, K, the concentration increase in Eq. (18) is also written as

$$\Delta C_p = K\Delta t. \tag{19}$$

By equating the right-hand side terms of Eqs. (18) and (19), the equation of the PM$_{2.5}$ mass mixing ratio at a grid cell after the emission process within a model time step is described by the following equation

$$\phi_{p2} = \phi_{p1}(\rho_{d1}/\rho_{d2}) + K\Delta t/\rho_{d2}. \tag{20}$$

If we assume the dry air density stays as a constant during the emission process within a single time step of Δt, Eq. (20) can be simplified as

$$\phi_{p2} = \phi_{p1} + K\Delta t/\rho_{d1}, \tag{21}$$

which is the equation we applied to represent the PM$_{2.5}$ emission process during each time step of the RK3 integration in the WRF model.

In our simulation, the initial PM$_{2.5}$ concentration was set to be zero everywhere. PM$_{2.5}$ pollutant was continuously added into the computational domain during each time step within a large square region covering the entire urban areas of the Beijing city. The region locates in the center of our inner domain and has a horizontal dimension of 120×120 km^2. In the vertical direction, it is within about the first 500 m
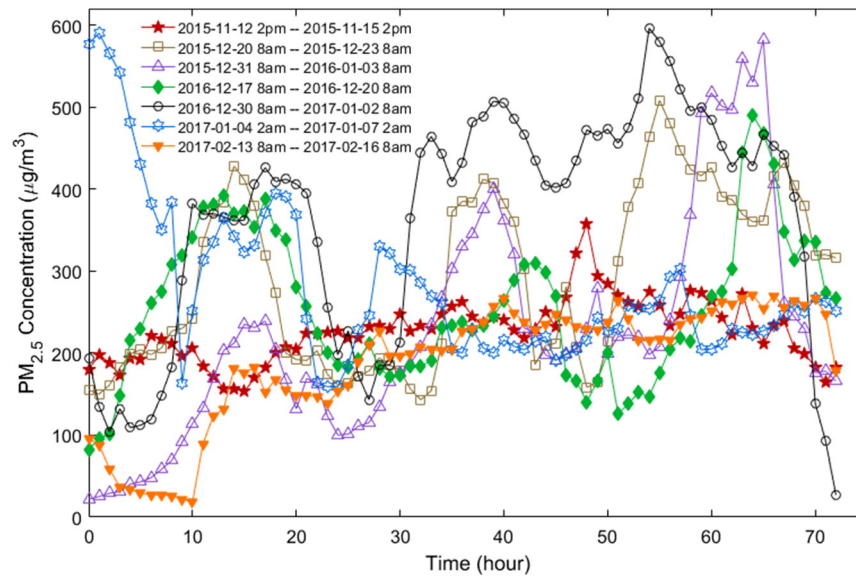
Fig. 4. Real-time PM$_{2.5}$ concentration data of Beijing measured at the U.S. embassy of China vs. time during seven air pollution episodes of the Beijing city provided by the U.S. Department of State. (http://www.stateair.net). The times shown are the Beijing local time.

above the ground. Thus, an air pollution field of PM$_{2.5}$ pollutant was generated in the current WRF model.

5. PM$_{2.5}$ pollutant cleaning effect of SALSCS

The eight full-scale SALSCSs clean up PM$_{2.5}$ pollutant in the model domain continuously during our simulations. Here, we present the method of calculating the cleaning effect of SALSCS on the air pollution field. As introduced previously, the SALSCS collector is represented by the nine grid cells on the lowest model level at each system location, with the nine grid cells having a total horizontal dimension of 3×3 km^2. In the vertical direction, the mass points on the lowest model level have a height of about 25 m above the earth ground. Here the nine grid cells are considered as a united control volume. It was assumed that each SALSCS cleans up PM$_{2.5}$ pollutant inside this control volume during each model time step. With a total volumetric value of V_{CV}, the control volume has its mass of dry air written in the following equation

$$m_{d,CV} = \rho_{d,CV} V_{CV}, \tag{22}$$

where the subscript, CV, indicates properties of the control volume. If the PM$_{2.5}$ pollutant mass mixing ratio is $\phi_{p,CV}$, the total pollutant mass inside the control volume equals to

$$m_{p,CV} = \phi_{p,CV} m_{d,CV} = \phi_{p,CV} \rho_{d,CV} V_{CV}. \tag{23}$$

During the SALSCS cleaning process within a model time step, Δt, the total PM$_{2.5}$ pollutant mass reduction within the control volume is

Table 3
Average PM$_{2.5}$ emission rates for the seven air pollution episodes in Beijing.

Local time of Beijing during each air pollution episode	Average PM$_{2.5}$ emission rate (μg/m^3-s)
2015-11-12 2:00 pm–2015-11-15 2:00 pm	4.91×10^{-3}
2015-12-20 8:00 am–2015-12-23 8:00 am	8.46×10^{-3}
2015-12-31 8:00 am–2016-01-03 8:00 am	6.53×10^{-3}
2016-12-17 8:00 am–2016-12-20 8:00 am	6.33×10^{-3}
2016-12-30 8:00 am–2017-01-02 8:00 am	7.08×10^{-3}
2017-01-04 2:00 am–2017-01-07 2:00 am	6.25×10^{-3}
2017-02-13 8:00 am–2017-02-16 8:00 am	4.06×10^{-3}

written as

$$\Delta m_{p,CV} = m_{p,CV1} - m_{p,CV2} = \left(\phi_{p,CV} \rho_{d,CV} V_{CV} \right)_1 - \left(\phi_{p,CV} \rho_{d,CV} V_{CV} \right)_2. \tag{24}$$

where subscripts of 1 and 2 indicate control volume properties before and after the cleaning process, respectively. This mass reduction term is also expressed in terms of the system volumetric flow rate, Θ,

$$\Delta m_{p,CV} = \int_t^{t+\Delta t} C_{p,CV}(t) \Theta dt, \tag{25}$$

where $C_{p,CV}$ means the PM$_{2.5}$ mass concentration in the control volume, which is a function of time. As SALSCS reduces air pollutant continuously, the pollutant concentration in the control volume decreases with time. To make it simpler, here we assumed that during each model time step this variable stays as a constant as the initial concentration value before the cleaning process, $C_{p,CV1}$, so that Eq. (25) is re-written as

$$\Delta m_{p,CV} = C_{p,CV1} (\Theta \Delta t) \tag{26}$$

As referred to Eq. (17), the mass concentration in Eq. (26) is formulated as

$$C_{p,CV1} = \frac{\left(\phi_{p,CV} m_{d,CV} \right)_1}{V_{CV1}} = \left(\phi_{p,CV} \rho_{d,CV} \right)_1 \tag{27}$$

It is straightforward that the terms on the right-hand sides of Eqs. (24) and (26) should be equal, from which the mass mixing ratio of PM$_{2.5}$ pollutant inside the control volume after the cleaning process of SALSCS within a time step is derived as

$$\phi_{p,CV2} = \frac{1}{\left(\rho_{d,CV} V_{CV} \right)_2} \left[\left(\phi_{p,CV} \rho_{d,CV} V_{CV} \right)_1 - \Theta \Delta t \left(\phi_{p,CV} \rho_{d,CV} \right)_1 \right]. \tag{28}$$

The height of the control volume, V_{CV}, changes slightly with time, because the WRF model has a vertical coordinate given by Eq. (16), instead of a Cartesian vertical coordinate. We assumed that both the dry air density and control volume in Eq. (28) stay constant during a time step, Δt,

which simplifies Eq. (28) to be

$$\phi_{p,CV2} = \left(1 - \frac{\Theta \Delta t}{V_{CV1}}\right)\phi_{p,CV1}. \tag{29}$$

The above equation was applied to calculate the PM$_{2.5}$ mass mixing ratio after the cleaning process within each time step of our WRF model. To be noted, through the derivation of Eq. (29), there is a hypothesis that the PM$_{2.5}$ pollutant is perfectly mixed within the control volume so that the pollutant mass concentration $C_{p,CV}$ is uniform throughout the nine grid cells during the cleaning process of each model time step.

6. Method of including SALSCS clean air

SALSCS delivers clean air (with zero PM$_{2.5}$ concentration based on our assumption) into the surrounding atmosphere through its tower outlet after PM$_{2.5}$ are separated from the system airflow by filtration elements. Here, we would like to trace the clean air of SALSCS and provide an estimation of the amount of clean air reaching the ground level of the Beijing urban area. Same as the treatment on PM$_{2.5}$ pollutant, passive tracer scalar, ϕ_c, presenting the mass mixing ratio of the clean air to dry air of the model, was applied to simulate the clean air emitted from the SALSCS tower, where the subscript, c, implies model properties related to clean air.

As mentioned previously, the SALSCS tower is represented by a column of grid cells located at the middle of the solar collector with a height of about 120 m. We assumed that the system clean air is released within the grid cell at the top of the grid column, which is considered as a control volume as well, and is added into the WRF model during each time step of the RK3 integration. Then the clean air mass of the control volume is calculated as

$$m_{c,CV} = \phi_{c,CV}m_{d,CV} = \phi_{c,CV}\rho_{d,CV}V_{CV}, \tag{30}$$

where the subscript of CV indicates parameters of the control volume. The increase of clean air inside the control volume within a model time step, Δt, is written as

$$\Delta m_{c,CV} = m_{c,CV2} - m_{c,CV1} = (\phi_{c,CV}\rho_{d,CV}V_{cv})_2 - (\phi_{c,CV}\rho_{d,CV}V_{CV})_1, \tag{31}$$

where subscripts 1 and 2 indicate variables before and after the clean-air emitting process, respectively. The term calculated by Eq. (31) is also related to the system flow rate, Θ, and clean air density, ρ_c, by the following equation

$$\Delta m_{c,CV} = (\Theta \Delta t)\rho_c. \tag{32}$$

From Eqs. (31) and (32), the equations for calculating the clean air mass mixing ratio after the emitting process, $\phi_{c,CV2}$, is derived as

$$\phi_{c,CV2} = \frac{1}{(\rho_{d,CV}V_{CV})_2}\left[(\phi_{c,CV}\rho_{d,CV}V_{CV})_1 + (\Theta \Delta t)\rho_c\right]. \tag{33}$$

It was assumed that the clean air coming out of the SALSCS tower has the same density as its surrounding ambient dry atmosphere within the control volume, and both the dry air density and our control volume stay constant during the emitting process within each time step, Δt. Therefore, we re-write Eq. (33) into a simpler form as follows

$$\phi_{c,CV2} = \phi_{c,CV1} + \frac{\Theta \Delta t}{V_{CV1}}. \tag{34}$$

This is the equation for calculating the clean air mass mixing ratio after the emitting process during each time step of our WRF simulations.

7. Results and discussion

7.1. Advection-scheme tests on passive tracer scalars

An appropriate advection scheme for the passive tracer scalar is crucial to scalar conservation (Wang et al., 2009), which is important for our quantitative analysis on both the air pollution and clean air fields. Numerical tests on the scalar advection schemes have been performed. Taking PM$_{2.5}$ pollutant field as an example, if a certain amount of PM$_{2.5}$ pollutant is initialized at a specific location in our simulation domain, the total mass should not change with time until some of the pollutant is transported outside of the domain by meteorological winds. As indicated by Wang et al. (2009), the best combination of advection schemes for scalar transport is to apply 5th (3rd) order horizontal (vertical) accuracy with a monotonic flux limiter, which achieves the minimum numerical dispersion and diffusion errors compared with the other advection schemes available in WRF. Our test model configuration is the same as described in the model configuration section. PM$_{2.5}$ pollutant was initialized with a uniform concentration of 200 μg/m^3 inside a large square region with a horizontal dimension of 120 × 120 km^2 at the center of the computation domain, and vertically the pollutant was initialized within the first 500 m above the ground. The model started at 00:00 (Coordinated Universal Time, UTC) on 2016-01-01, and the results within the first 3 h into the simulation were obtained before any pollutant transported across the domain boundaries. Different advection schemes combined with different flux limiters were tested in this study. Fig. 5 shows the conservation performance of the tracer scalar of PM$_{2.5}$ pollutant for each tested advection scheme within the first 3 h of the simulation. To be noted here, the depiction of symbols for the curves was for readers to easily follow rather than they were experimental data. For the same reason, symbols were also used in Figs. 6–9. The percentage on the y-axis indicates the divergence of the total PM$_{2.5}$ pollutant mass at each time level from the initial total mass, and is defined by the following equation

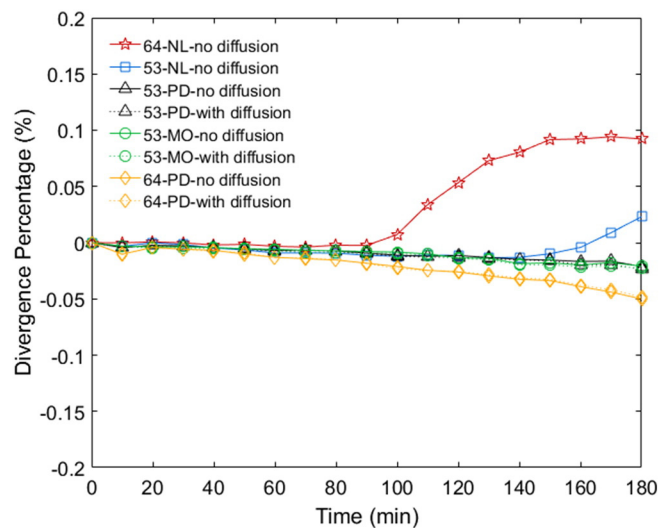$$P_{DV} = \frac{m_{tl} - m_{tot}}{m_{tot}}, \tag{35}$$

Fig. 5. Percentage, P$_{DV}$, of divergence from the initial total PM$_{2.5}$ mass within the model domain vs. time during the first 3 h into the simulations of the test cases with various advection schemes. 53 and 64 indicate 5th (3rd) and 6th (4th) order accuracy in the horizontal (vertical) direction, respectively. NL, PD and MO represent schemes with no flux limiter, positive-definite flux limiter and monotonic flux limiter, respectively; "no diffusion" and "with diffusion" indicate diffusion terms for the unresolved turbulent energy dissipation are turned off and on, respectively.
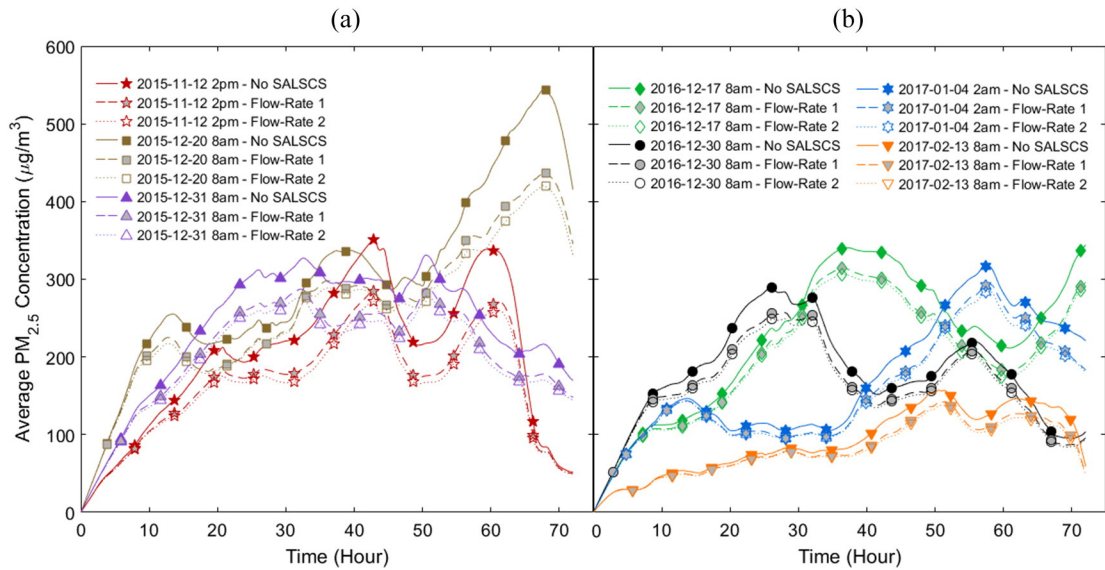
Fig. 6. Numerical results of PM$_{2.5}$ mass concentrations vs. time, averaged within a region of 120×120 km^2 over the Beijing city for the seven air pollution episodes during (a) the winter of 2015 and (b) the winters of 2016 and 2017, under three simulation conditions, (1) with no SALSCS, (2) with SALSCSs of Flow-Rate 1 and (3) with SALSCSs of Flow-Rate 2.

where m_{tot} is the initial total PM$_{2.5}$ mass in the entire model domain and m_{tl} is the total mass at each time level. The time resolution on the x-axis of Fig. 5 is 10 min. Two combinations of order of accuracy were tested, which are 5th (3rd) and 6th (4th) order accurate in the horizontal (vertical) direction as denoted by "53" and "64", respectively. "NL", "PD" and "MO" represent numerical advection schemes with no flux limiter, with positive-definite limiter and with monotonic flux limiter, respectively. The effect of diffusion terms on the conservation performance of the tracer scalar were also tested, which account for the turbulent energy dissipation under the unresolved model scale. In Fig. 5, "with diffusion" indicates the diffusion terms were considered during the simulation, while "no diffusion" means those terms were turned off in both the horizontal and vertical model directions simultaneously since the turbulent energy dissipation is parameterized separately in the two directions of the WRF model.

Our test results in Fig. 5 show that without a flux limiter, the total mass of the PM$_{2.5}$ pollutant within the entire domain starts to increase at a time of around 80 min for the "64-NL" scheme and 130 min for "53-NL". Thus, a flux limiter is necessary for our study to make sure the passive tracer scalar is well conserved. On the other hand, advection schemes with "53" order of accuracy give better conservation performance than schemes with "64". This is because the even-order

advection schemes in WRF is more dispersive than the odd-order schemes, with the latter causing more oscillations near the discontinuous regions of the tracer scalar field. Further explanations of this can be referred to Skamarock et al. (2008) and Wicker and Skamarock (2002). As indicated by the black and green curves in Fig. 5, advection schemes of "53-PD" and "53-MO" both work well for our scalar conservation purpose. The results suggest that within the first 3 h of simulation, the total mass of the PM$_{2.5}$ pollutant differs <0.03% from the initial value for both the two schemes, indicating that the two flux limiters do not affect the tracer-scalar conservation property significantly. Although the positive-definite (PD) flux limiter has little influence on the tracer-scalar conservation in general, numerical oscillations can still occur and produce dispersion errors in the scalar field as pointed out by Wang et al., 2009. The monotonic (MO) flux limiter corrects the dispersive numerical errors in general and keeps the diffusion errors at a minimum extent. By comparing the solid curves with the corresponding dashed curves, one can find the diffusion terms mentioned above have very little impact on the scalar conservation performance, so that they should be included in the WRF model to account for the turbulent energy dissipation of the unresolved scale. Therefore, the scalar advection scheme of "53-MO-with diffusion" as indicated by the green dashed curve with circle symbols in Fig. 5 was chosen for simulating the PM$_{2.5}$ pollutant over the terrain of Beijing in the current study.

7.2. PM$_{2.5}$ pollutant reduction by SALSCS

WRF simulations were conducted for the seven air pollution episodes of the Beijing city during the winters of 2015–2017, as presented in the previous Fig. 4. All the simulations here lasted for 72 h. Fig. 6(a) and (b) show the numerically-obtained PM$_{2.5}$ mass concentrations within the first 50 m above the earth's ground averaged over a square region with a horizontal dimension of 120×120 km^2, which entirely covers the urban areas of the Beijing city. Each air pollution episode in the two figures is represented by a unique color corresponding to the curve color in Fig. 4. The legends of Fig. 6(a) and (b) give the local Beijing time at the beginning of each air pollution episode. There are three curves presented for each case. The solid, dashed and dotted curves indicate the average PM$_{2.5}$ mass concentration profiles obtained from the WRF model when there is no SALSCS included in the computational domain, eight SALSCSs with Flow-Rate 1 included in the domain, and eight SALSCSs with Flow-Rate 2 included in the domain, respectively. Flow-Rates 1 and 2 are related to the SALSCS flow rates of 2.64×10^5 m^3/s
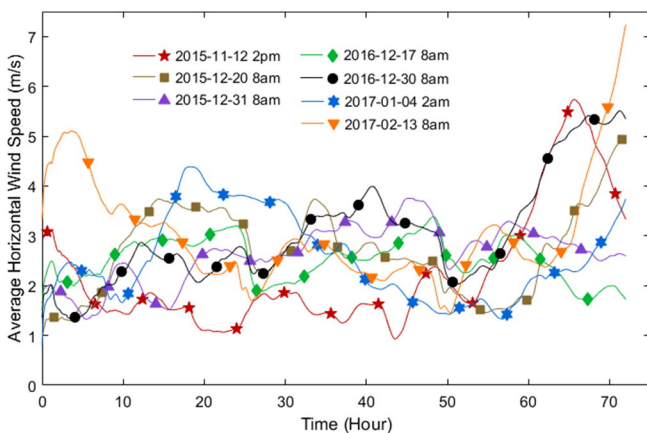

Fig. 7. Numerical results of horizontal wind speeds for the seven air pollution episodes vs. time, averaged at a height of 25 m above the earth's ground over the region of 120×120 km^2.
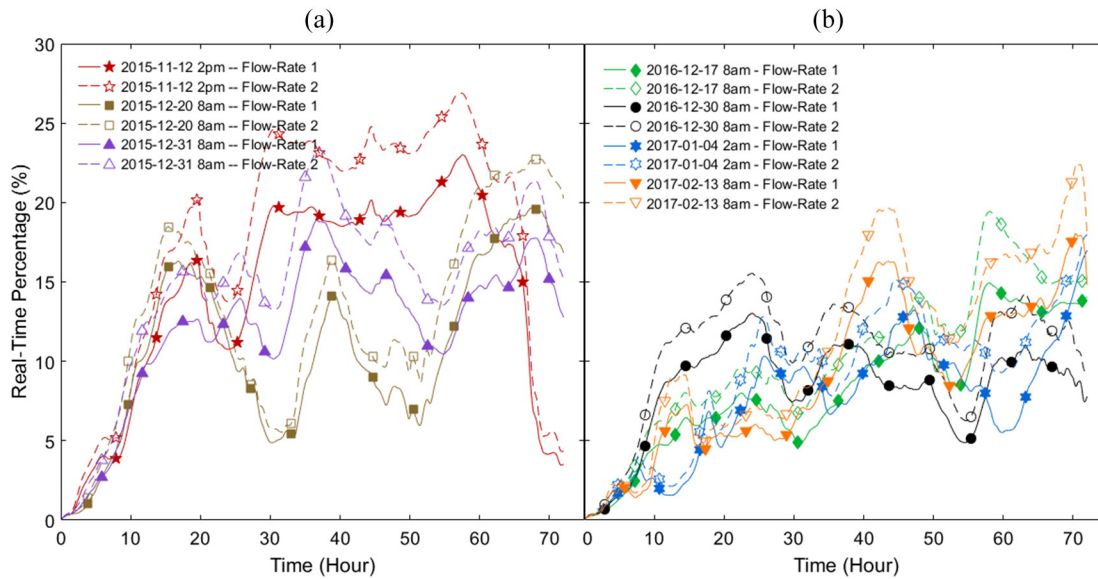
Fig. 8. Air-pollution reduction percentages of SALSCS vs. time under the two flow-rate conditions averaged within a region of $120 \times 120 \text{ km}^2$ for the seven air pollution episodes during (a) the winter of 2015 and (b) the winters of 2016 and 2017.

and $3.80 \times 10^5 \text{ m}^3/\text{s}$, respectively, which are the two system flow rates consistent with the work of Cao et al. (2015). According to Fig. 6(a) and (b), the average $PM_{2.5}$ concentration decreases as the SALSCS flow rate increases. For each air pollution episode, the initial mass concentration starts from zero since there was no pollutant at the beginning of each simulation. As shown in the two figures, during the first 24 h of each simulation, the concentration value increases with time in general. Thus, we used the first 24-hour period into each simulation as a spin-up time during which the $PM_{2.5}$ air pollutant field in our WRF model domain was fully generated. The numerical data of the later 48-hour period of each simulation was used to perform our results analysis for each simulated air pollution episode. Fig. 6 also shows that the WRF simulations obtain quite different air pollution fields with various $PM_{2.5}$ mass concentrations for the seven air pollution episodes. For instance, the case starting at 2017-02-13 8 am has a comparably low average mass concentration around 100 μg/m^3, while during the later period of case 2015-12-20 8 am, the average mass concentration increases to a

high value of 550 μg/m^3. One reason causing this difference is that the emission rates applied for the seven episodes are different as shown in Table 3. Cases of 2017-02-13 8 am and 2015-12-20 8 am have the highest and lowest $PM_{2.5}$ emission rates, respectively, among the seven pollution episodes. On the other hand, the meteorological condition is also important for the model-generated air pollution field. If the ambient wind speed is lower, the emitted $PM_{2.5}$ pollutant has a less tendency to be blown away so that it is easier for the pollutants to accumulate at one location causing a $PM_{2.5}$ field with higher mass concentration in the model domain.

Fig. 7 gives the horizontal wind speeds averaged at about 25 m above the ground as a function of time for the seven air pollution episodes, and in the horizontal direction they were averaged over the same region as the $PM_{2.5}$ pollutant mass concentration shown in Fig. 6 (a) and (b). The 72-hour averaged value of the horizontal wind speeds for the seven pollution episodes is 2.67 m/s. For cases of 2016-12-30 8 am, 2017-01-04 2 am and 2017-02-13 8 am, the wind speeds increase
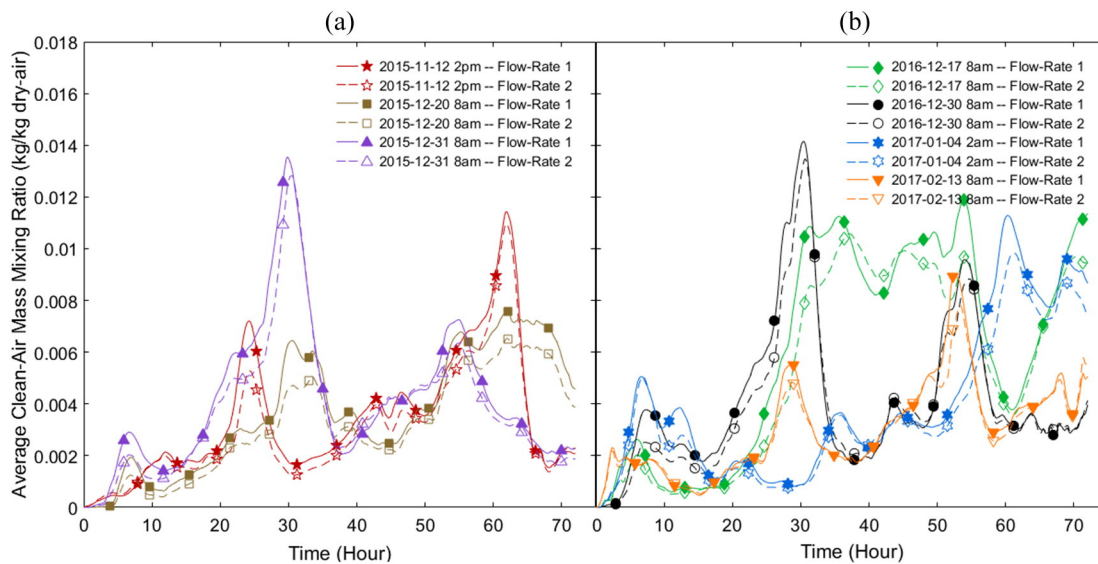

Fig. 9. Numerical results of SALSCS clean-air mass mixing ratios within about the first 50 m above the ground vs. time, averaged over a region of $60 \times 60 \text{ km}^2$ covering the downtown area inside the 6$^{\text{th}}$ Ring Road of the Beijing city for the seven air pollution episodes during (a) the winter of 2015 and (b) the winters of 2016 and 2017, under 2 simulation conditions with (1) eight SALSCSs of Flow-Rate 1 and (2) eight SALSCSs of Flow-Rate 2.

to relatively high values after about 60 h into the simulation, and the corresponding PM$_{2.5}$ mass concentration in Fig. 6(b) drops accordingly. For the case of 2016-12-17 8 am, when the wind speed decreases during the last 12 h of the simulation, the obtained PM$_{2.5}$ concentration starts to increase. These facts indicate that the calculated PM$_{2.5}$ concentration has an inverse correlation with the wind speed. However, the cases of 2015-11-12 2 pm, 2015-12-20 8 am and 2015-12-31 8 am indicate more complicated relationships between the PM$_{2.5}$ concentration and the average wind speed. Except for wind speed, there are many other factors that affect the PM$_{2.5}$ concentration. For example, the terrain shape and the wind direction could be quite important under certain conditions. For our situation, the computational domain over the Beijing city has mountains on the west and north and plains on the east and south, as shown by the previous Fig. 2. If the wind is blowing from the east to the west, the mountains on the west side of the city prevent the PM$_{2.5}$ pollutant from being further transported away, which makes it possible to cause higher local PM$_{2.5}$ concentration on the east side of the mountain regions. On the other hand, if westerly wind happens under the same wind speed, the result would be quite different. This is because no obstacle appears on the east of the city, and the PM$_{2.5}$ pollutant is blown away quickly by the wind, which may lead to an air pollution field with lower concentration. These interesting phenomena should be studied in detail for future research and was not covered by the current work.

The real-time percentages in Fig. 8(a) and (b) illustrate how much PM$_{2.5}$ pollutant is reduced by the eight SALSCSs installed in our model domain, which is a function of time and differs case by case. The legends of the figures indicate the local starting times of the seven simulation scenarios. The solid and dashed curves for each air pollution episode present the percentage distributions under simulation conditions with SALSCS Flow-Rates 1 and 2, respectively. This air-pollution reduction percentage is defined as

$$P_r = \frac{C_{NS} - C_{WS}}{C_{NS}} \qquad (36)$$

where C_{NS} and C_{WS} are the calculated average PM$_{2.5}$ mass concentrations under the conditions without and with SALSCSs, respectively, which have been shown in Fig. 6(a) and (b). With a higher system flow rate of Flow-Rate 2, the modeling results achieve a higher air pollution reduction percentage for each of the seven air pollution episodes than the results under the condition of Flow-Rate 1. Since the first 24 h of each simulation was considered as a spin-up time, we only analyzed the percentage results during the later 48 h for each air pollution episode. By averaging the percentages in Fig. 8(a) and (b) over the later 48-hour simulation period for all of the seven cases together, it was found that the average pollution reduction percentage by the eight SALSCSs equals to 11.9% under the Flow-Rate 1 condition, and 14.6% under the Flow-Rate 2 condition. It's obvious that if we keep increasing the system flow rate by operating more powerful fans or installing more SALSCSs in the surrounding areas of the city, the reduction percentage of PM$_{2.5}$ by SALSCSs over the Beijing terrain can be further increased.

As shown in both Fig. 8(a) and (b), the average reduction percentages vary with time significantly, indicating that the ability of the eight SALSCSs in controlling air pollution over the Beijing city depends not only on their system flow rate but also the surrounding ambient environment. For instance, the air-pollution reduction percentages of SALSCS can be affected by meteorological wind condition. Fig. 8(a) shows that the case of 2015-11-12 2 pm has a pollution reduction percentage as high as 19.6% and 23.7% under the conditions of Flow-Rate 1 and 2, respectively, between the simulation time of 30 h and 57 h, after which the percentage drops quickly. The corresponding average wind speed, as shown in Fig. 7, is 1.72 m/s during the same period of 30–57 h, which is relatively low compared with other time periods, and increases rapidly after it. In addition, the case of 2016-12-30 8 am in Fig. 8(b) has the lowest pollution reduction percentages of 9.0% and 11.4%

for the two flow-rate conditions, respectively, during the later 48-hour simulation period, and meanwhile, it has the highest average wind speed among the seven episodes which is equal to 3.45 m/s. Although many factors in the surrounding environment of SALSCS may influence its air-pollution cleaning ability, the wind condition is one of the key factors. During a low-wind period, the SALSCS is operated within a relatively stable air-pollution field, which makes the system possible to access a large amount of air pollutants and to have a strong impact on reducing the air pollution of the city. Under a high-wind situation, however, the wind may blow the air pollutants away from the surrounding areas of SALSCS, causing the air pulled into the system solar collector to have low air pollution concentration so that only a small amount of air pollutant is collected by the filtration elements. Research work should be further carried out to answer questions such as how SALSCS could operate with a better efficiency in controlling air pollution under various meteorological conditions.

7.3. SALSCS-emitted clean air

SALSCS delivers clean air into the nearby atmosphere through its tower, which is carried around over the city terrain by meteorological winds. If the clean-air flow reaches the atmospheric region close to the ground level of the populous downtown area, the urban residents would benefit from it. Fig. 9(a) and (b) show the numerically obtained mean clean-air mass mixing ratios within the first 50 m above the ground during the seven air pollution episodes, which were averaged over a 60×60 km^2 area covering the downtown of Beijing encompassed by the 6th Ring Road of the city. Solid and dashed curves with full and open symbols indicate the mixing-ratio distributions versus simulation time for the two modeling conditions. As shown in the figures, the obtained mass mixing ratios are very small, below 0.015 for all cases, implying that only a small amount of the emitted clean air in the atmosphere finally reaches the downtown region of Beijing, and the current configuration of SALSCS is not efficient in delivering its clean air back to the populous urban area. There are two reasons contributing to this fact. First, the clean air leaving the outlet of a SALSCS tower has an upward velocity. This vertical momentum carries the clean-air flow further into a higher level of the atmosphere. Second, solar energy heats the airflow inside SALSCS, so that the clean air at the system outlet has a higher temperature, and correspondingly, a lower density than the surrounding environment. In this regard, buoyancy force leads to an extra tendency for upward motion for the emitted clean air. The small clean-air portion finally reaching the ground level is transported mainly by the atmospheric turbulence dispersion (Seinfeld and Pandis, 2006) if there is no downward flow in the atmosphere, while most of the emitted clean air stays at higher levels of the atmosphere and does not approach the ground at all.

The clean-air mass mixing ratios for the seven pollution episodes in both Fig. 9(a) and (b) were averaged together during the later 48-hour simulation period to be 5.22×10^{-3} and 4.74×10^{-3} for Flow-Rates 1 and 2, respectively. Interestingly, under the current simulation conditions, a higher system flow rate gives a smaller amount of clean air reaching the ground level. This conclusion is also clearly demonstrated in both figures by comparing the two curves for each pollution episode. During most of the simulation time, the solid curve is on top of the corresponding dashed curve, indicating that the mass mixing ratio under Flow-Rate 1 is larger than the mixing ratio under Flow-Rate 2. This can also be explained by the two reasons mentioned above. A higher system flow rate is related to a higher clean-air vertical momentum and lower air density so that the clean-air plume flows up further into the atmosphere. However, as indicated by Fig. 9(a) and (b), the mass mixing ratio under Flow-Rate 1 can also be smaller than the mixing ratio under Flow-Rate 2 occasionally during some circumstances, which is caused by the larger amount of clean air delivered by SALSCSs with the latter simulation condition.

For each of the seven air pollution episodes, Fig. 10 presents a snapshot of the numerical contours of the clean-air mass mixing ratio
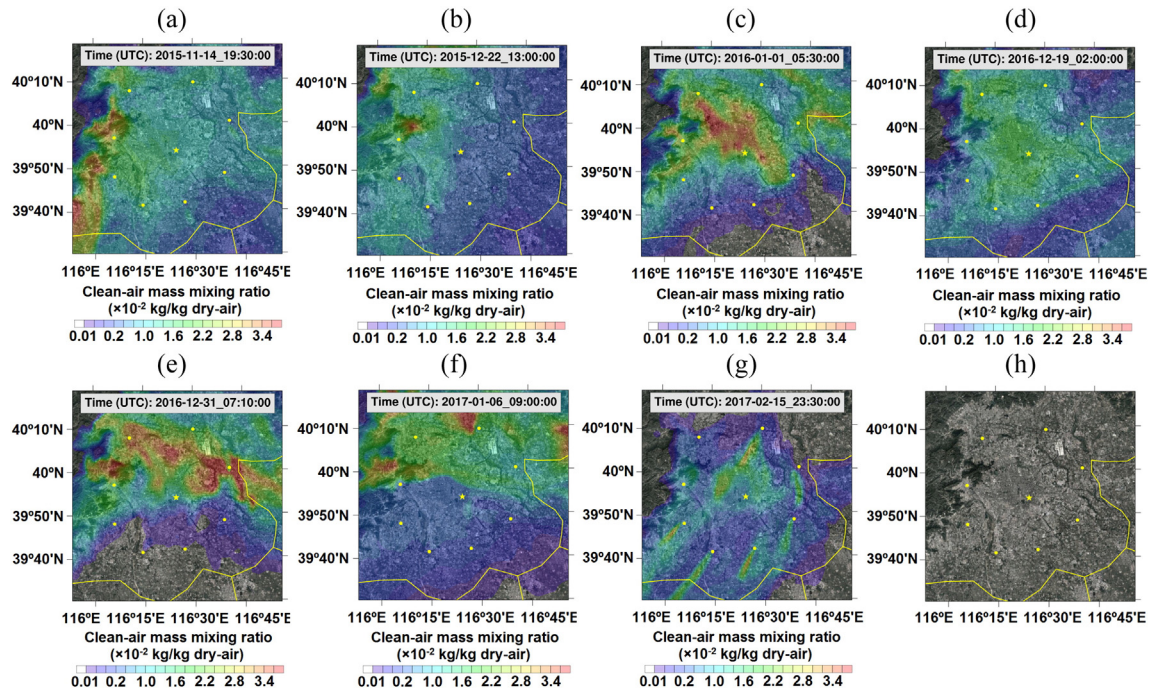
Fig. 10. Snapshots of numerical contours of SALSCS clean-air mass mixing ratios within about the first 50 m above the ground for the seven air pollution episodes of (a) 2015-11-12 2 pm, (b) 2015-12-20 8 am, (c) 2015-12-31 8 am, (d) 2016-12-17 8 am, (e) 2016-12-30 8 am, (f) 2017-01-04 2 am, and (g) 2017-02-13 8 am. Shown are the contours obtained under the simulation condition of Flow-Rate 1. Fig. (h) presents the satellite picture of the Beijing city overlaid by the numerical contours.

averaged within the first 50 m above the ground under the simulation condition of Flow-Rate 1 (2.64 × 10^5 m^3/s). The contours were overlaid above a satellite picture of the city as shown by Fig. 10(h), where details of the Beijing downtown and its surrounding area are displayed. The horizontal dimension of the picture is about 100 × 100 km^2. The downtown area located at the domain center is denoted by a yellow star, while the eight yellow dots indicate the locations of SALSCSs. The yellow lines show the province boundaries of the area. Coordinated Universal Time (UTC) of each snapshot is given in the time label at the top of each figure, which is 8 h behind the Beijing local time. The seven snapshots show different occasions when there is clean air covering the downtown region of the city, where blue and red colors indicate lower and higher values of the clean-air mass mixing ratio, respectively. The transparent color is applied if the mass mixing ratio is lower than 10^{-4}. Fig. 10 presents various patterns of clean-air distributions over the

city of Beijing. Fig. 10(a) and (d) show that the clean air has a uniform distribution in general over the downtown area, while a higher amount of clean air on the west and southwestern corner is also shown in Fig. 10 (a). In Fig. 10(b), the west side of the city has a higher clean-air mixing ratio in average than the east side. As shown by Fig. 10(c), the central and northern part of the downtown area has relatively higher clean air concentrations than the other surrounding areas. Both Fig. 10(e) and (f) indicate that the clean air is concentrated on the north side of the city. In Fig. 10(g), a few clean air plumes appear at the downwind locations of the SALSCS, contributing to a higher clean-air mass mixing ratio near the central and southwest part of the city.

To better understand how the SALSCS clean air is transported over the Beijing terrain, 3-D renderings of the clean-air plumes were produced. Fig. 11(a)–(g) shows the snapshots of the 3-D clean-air fields in white color, which are relative to the 2-D contours in Fig. 10. In
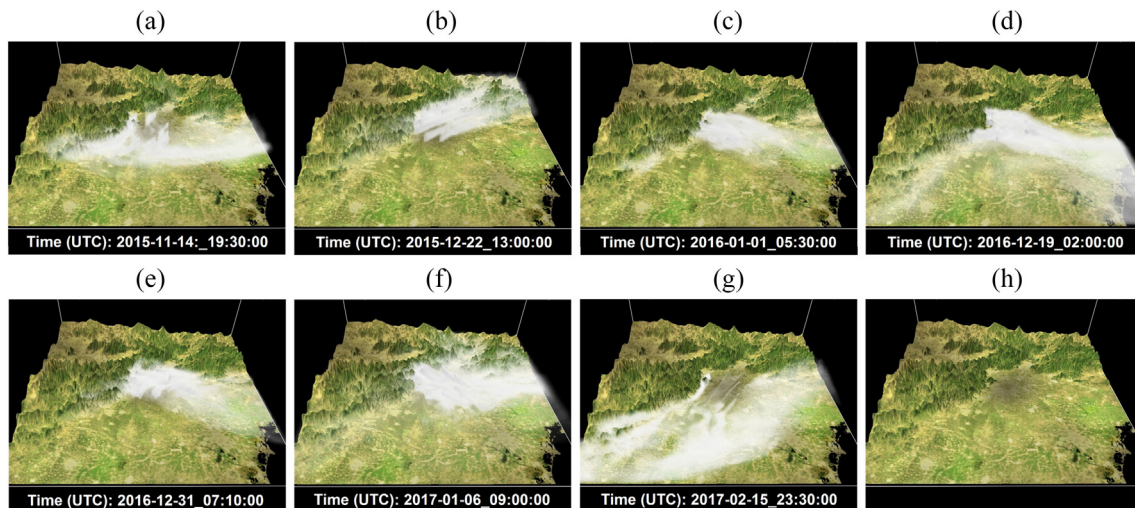

Fig. 11. Snapshots of clean-air fields from the simulations of the seven air pollution episodes, corresponding to the contours in Fig. 10. Shown are the 3-D fields of the clean-air mass mixing ratios as displayed in white. Fig. 11(h) gives the terrain shape of the WRF computational domain.

each snapshot of Fig. 11, we look into the north direction of the domain, and vertically it was stretched by 15 times so that clean air plumes can be observed clearly. The terrain geometry is presented by Fig. 11(h). As indicated by these snapshots, most of the clean air emitted by the eight SALSCSs stays high in the atmosphere during the simulations.

8. Summary and future work

In this paper, we introduced the WRF model for evaluating the effect of a full-scale Solar-Assisted Large-Scale Cleaning System, SALSCS, initially proposed by Cao et al. (2015), on remediating the air pollution problem of the Beijing city in China. Eight SALSCSs installed along the 6th Ring Road of the city were considered in our model domain. An extra tendency term was applied to the potential temperature equation to simulate the buoyancy effect generated by SALSCS on the nearby atmosphere. $PM_{2.5}$ pollutant was included to create an air-pollution field in the model based on the emission rates evaluated according to the real-time $PM_{2.5}$ concentration data available on the website attributing to the U.S. Department of State. Passive tracer scalars were applied to simulate the $PM_{2.5}$ pollutant and clean air delivered by the SALSCSs. Meanwhile, methods of generating the $PM_{2.5}$ pollution field, calculating the effectiveness of SALSCS on reducing $PM_{2.5}$ pollutant and determining the amount of SALSCS clean air reaching the ground level in the WRF model have all been presented and discussed in this paper.

Numerical simulations under two different SALSCS flow-rate conditions of Flow-Rates 1 and 2 (2.64×10^5 m^3/s and 3.80×10^5 m^3/s, respectively) were conducted to evaluate the pollution reduction percentages during seven air pollution episodes of the Beijing city. As indicated by our results, the average $PM_{2.5}$ reduction percentage is 11.9% under the condition of Flow-Rate 1 and 14.6% with Flow-Rate 2. Ambient factors, such as meteorological wind condition, affecting the obtained $PM_{2.5}$ concentration fields and pollution reduction percentages of SASCLS were discussed. Clean-air mass mixing ratio within the first 50 m above the earth's ground averaged through the seven air pollution episodes equals to 5.22×10^{-3} and 4.74×10^{-3} (kg/kg dry-air) under the simulation conditions of Flow-Rates 1 and 2, respectively, indicating that the current SALSCS configuration has a small efficiency in delivering its clean air to the downtown area of the city. It was shown that the higher Flow-Rate 2 results in less amount of clean air reaching the ground level in general, which is caused by the higher airflow velocity at the system outlet and stronger buoyancy effect on the emitted clean air under the condition of a higher flow rate. 2-D contours and 3-D renderings of the clean air fields have also been displayed at the end of the Results and discussion section.

As discussed previously, the proposed full-scale SALSCS with a large solar collector can only be installed in the suburb regions of a city where lands for constructions are available. With this configuration, the current study indicates that the system efficiency in delivering its clean air to the downtown area needs to be improved. The solution may be to install mid-scale SALSCSs directly inside the downtown region of a city. In the future, research should be conducted to improve system performance on provisioning of its clean air for the city population and developing methods of operational control of the system under various meteorological conditions and surrounding environments.

Nomenclature

A	area occupied by the solar collector of SALSCS, m^2
C	concentration, $\mu g/m^3$
c_p	specific heat at constant pressure, J/kg-K
c_v	specific heat at constant volume, J/kg-K
F	tendency term added onto the potential temperature equation, K/s
f	mapping factor
g	gravitational acceleration, m/s^2
K	$PM_{2.5}$ emission rate, $\mu g/m^3$-s
m	air mass, kg

P	percentage, %
p	pressure, Pa
p_0	reference pressure, 10^5 Pa
Q	solar heating rate per unit dry air mass, J/kg-s
q	solar heat flux, W/m^2
R	specific gas constant of dry air, J/kg-K
T	temperature, K
t	simulation time, s
u	velocity component in x direction, m/s
V	volume, m^3
v	velocity component in y direction, m/s
w	velocity component in z direction, m/s

Greek

Δt	time step of the RK3 integration, s
Δx	grid spacing in x-direction, m
Δy	grid spacing in y-direction, m
η	vertical coordinate of the WRF model
Θ	SALSCS volumetric flow rate, m^3/s
θ	potential temperature, K
μ	mass per unit area of a model column, Pa
ρ	air density, kg/m^3
ϕ	mass mixing ratio, kg/kg dry-air

Subscripts

1	properties before a modeling process
2	properties after a modeling process
CV	control volume
c	clean air
DV	divergence
d	dry air
g	grid cell
h	hydrostatic
NS	without SALSCS
p	air pollutant
r	reduction
s	bottom of the simulated atmosphere
t	top of the simulated atmosphere
tl	time level
tot	total
WS	with SALSCS
x	in x-direction
y	in y-direction

Appendix A. Supporting information

Supporting information to this article can be found online at https://doi.org/10.1016/j.scitotenv.2018.01.062.

References

Ahmadov, R., McKeen, S., Trainer, M., Banta, R., Brewer, A., Brown, S., Edwards, P.M., Gouw, J.A., Frost, G.J., Gilman, J., Helmig, D., Johnson, B., Karion, A., Koss, A., Langford, A., Lerner, B., Olson, J., Oltmans, S., Peischl, J., Pétron, G., Pichugina, Y., Roberts, J.M., Ryerson, T., Schnell, R., Senff, C., Sweeney, C., Thompson, C., Veres, P.R., Warneke, C., Wild, R., Williams, E.J., Yuan, B., Zamora, R., 2015. Understanding high wintertime ozone pollution events in an oil and natural gas-producing region of the western US. Atmos. Chem. Phys. 15, 411–429.

Al-Kayiem, H.H., Aja, O.C., 2016. Historic and recent progress in solar chimney power plant enhancing technologies. Renew. Sust. Energ. Rev. 58, 1269–1292.

Arakawa, A., Lamb, V., 1977. Computational design of the basic dynamical processes of the UCLA General Circulation Model. Methods in Computational Physics. 17. Academic Press, pp. 173–265.

Beck, V., Gerbig, C., Koch, T., Bela, M.M., Longo, K.M., Freitas, S.R., Kaplan, J.O., Bergamaschi, P., Heimann, M., 2013. WRF-Chem simulations in the Amazon region during wet and dry season transitions: evaluation of methane models and wetland inundation maps. Atmos. Chem. Phys. 13, 7961–7982.

Cao, Q., Pui, D.Y.H., Lipiński, W., 2015. A concept of a novel solar-assisted large-scale cleaning system (SALSCS) for urban air remediation. Aerosol Air Qual. Res. 15, 1–10.

Chen, F., Dudhia, J., 2001a. Coupling an advanced land surface-hydrology model with the Penn State–NCAR MM5 modeling system. Part I: model implementation and sensitivity. Mon. Weather Rev. 129, 569–585.

Chen, F., Dudhia, J., 2001b. Coupling an advanced land surface-hydrology model with the Penn State–NCAR MM5 modeling system. Part II: preliminary model validation. Mon. Weather Rev. 129, 587–604.

Chen, Y., Ebenstein, A., Greenstone, M., Li, H., 2013a. Evidence on the impact of sustained exposure to air pollution on life expectancy from China's Huai River policy. Proc. Natl. Acad. Sci. U. S. A. 110, 12936–12941.

Chen, D., Li, Q., Stutz, J., Mao, Y., Zhang, L., Pikelnaya, O., Tsai, J.Y., Haman, C., Lefer, B., Rappenglück, B., Alvarez, S.L., Neuman, J.A., Flynn, J., Roberts, J.M., Nowak, J.B., de Guow, J., Holloway, J., Wagner, N.L., Veres, P., Brown, S.S., Ryerson, T.B., Warneke, C., Pollack, I.B., 2013b. WRF-Chem simulation of NO$_x$ and O$_3$ in the L.A. Basin during CalNex-2010. Atmos. Environ. 81, 421–432.

Clyne, J., Rast, M., 2005. A prototype discovery environment for analyzing and visualizing terascale turbulent fluid flow simulations. Proc. Vis. Data Anal. 284–294 2005.

Clyne, J., Mininni, P., Norton, A., Rast, M., 2007. Interactive desktop analysis of high resolution simulations: application to turbulent plume dynamics and current sheet formation. New J. Phys. 9, 301.

Dudhia, J., 1989. Numerical study of convection observed during the winter monsoon experiment using a mesoscale two-dimensional model. J. Atmos. Sci. 46, 3077–3107.

Ek, M.B., Mitchell, K.E., Lin, Y., Rogers, E., Grunmann, P., Koren, V., Gayno, G., Tarpley, J.D., 2003. Implementation of Noah land surface model advances in the National Centers for Environmental Prediction operational mesoscale eta model. J. Geophys. Res. 108, 8851.

Fasel, H.F., Meng, F., Shams, E., Gross, A., 2013. CFD analysis for solar chimney power plants. Sol. Energy 98, 12–22.

Grell, G.A., Freitas, S.R., 2013. A scale and aerosol aware stochastic convective parameterization for weather and air quality modeling. Atmos. Chem. Phys. Discuss. 13, 23845–23893.

Grell, G.A., Peckham, S.E., Schmitz, R., McKeen, S.A., Frost, G., Skamarock, W.C., Eder, B., 2005. Fully coupled "online" chemistry within the WRF model. Atmos. Environ. 39, 6957–6975.

Haaf, W., 1984. Solar chimneys, part II: preliminary test results from the Manzanares pilot plant. Int. J. Sol. Energy 2, 141–161.

Haaf, W., Friedrich, K., Mayr, G., Schlaich, J., 1983. Solar chimneys, part I: principle and construction of the pilot plant in Manzanares. Int. J. Sol. Energy 2, 3–20.

Hao, J., Wang, L., Shen, M., Li, L., Hu, J., 2007. Air quality impacts of power plant emissions in Beijing. Environ. Pollut. 147, 401–408.

Hong, S.-Y., Lim, J.-O.J., 2006. The WRF single-moment 6-class microphysics scheme (WSM6). J. Korean Meteor. Soc. 42, 129–151.

Hong, S.-Y., Noh, Y., Dudhia, J., 2006. A new vertical diffusion package with explicit treatment of entrainment processes. Mon. Weather Rev. 134, 2318–2341.

Jiang, F., Wang, T., Wang, T., Xie, M., Zhao, H., 2008. Numerical modeling of a continuous photochemical pollution episode in Hong Kong using WRF-Chem. Atmos. Environ. 42, 8717–8727.

Jiménez, P.A., Dudhia, J., González-Rouco, J.F., Navarro, J., Montávez, J.P., García-Bustamante, E., 2012. A revised scheme for the WRF surface layer formulation. Mon. Weather Rev. 140, 898–918.

Kampa, M., Castanas, E., 2008. Human health effects of air pollution. Environ. Pollut. 151, 362–367.

Kasaeian, A.B., Molana, S., Rahmani, K., Wen, D., 2017. A review on solar chimney systems. Renew. Sust. Energ. Rev. 67, 954–987.

Kundu, P.K., Cohen, I.M., Dowling, D.R., 2011. Fluid Mechanics. Fifth Edition. Academic Press, Cambridge, MA.

Kusaka, H., Kimura, F., 2004. Coupling a single-layer urban canopy model with a simple atmospheric model: impact of urban heat island simulation for an idealized case. J. Meteor. Soc. Japan. 82, 67–80.

Kusaka, H., Kondo, H., Kikegawa, Y., Kimura, F., 2001. A simple single-layer urban canopy model for atmospheric models: comparison with multi-layer and SLAB models. Bound.-Layer Meteorol. 101, 329–358.

Laprise, R., 1992. The Euler equations of motion with hydrostatic pressure as an independent variable. Mon. Weather Rev. 120, 197–207.

Mao, X., Zhou, J., Corsetti, G., 2014. How will have China's recent five-year plans been implemented for energy conservation and air pollution control? Environ. Sci. Technol. 48, 10036–10044.

Matsui, H., Koike, M., Kondo, Y., Takegawa, N., Fast, J.D., Pöschl, U., Garland, R.M., Andreae, M.O., Wiedensohler, A., Sugimoto, N., Zhu, T., 2010. Spatial and temporal variations of aerosols around Beijing in summer 2006: 2. Local and column aerosol optical properties. J. Geophys. Res. 115, D22207.

Ming, T., Liu, W., Pan, Y., Xu, G., 2008. Numerical analysis of flow and heat transfer characteristics in solar chimney power plants with energy storage layer. Energ. Convers. Manag 49, 2872–2879.

Mlawer, E.J., Taubman, S.J., Brown, P.D., Iacono, M.J., Clough, S.A., 1997. Radiative transfer for inhomogeneous atmosphere: RRTM, a validated correlated-k model for the long wave. J. Geophys. Res. 102, 16663–16682.

Pastohr, H., Kornadt, O., Gürlebeck, K., 2004. Numerical and analytical calculations of the temperature and flow field in the upwind power plant. Int. J. Energy Res. 28, 495–510.

Pasumarthi, N., Sherif, S.A., 1998a. Experimental and theoretical performance of a demonstration solar chimney model – part I: mathematical model development. Int. J. Energy Res. 22, 277–288.

Pasumarthi, N., Sherif, S.A., 1998b. Experimental and theoretical performance of a demonstration solar chimney model – part II: experimental and theoretical results and economic analysis. Int. J. Energy Res. 22, 443–461.

Pretorius, J.P., Kröger, D.G., 2006. Critical evaluation of solar chimney power plant performance. Sol. Energy 80, 535–544.

Pui, D.Y.H., Chen, S.-C., Zuo, Z., 2014. PM$_{2.5}$ in China: measurements, sources, visibility and health effects, and mitigation. Particuology. 13, 1–26.

Schlaich, J., Bergermann, R., Schiel, W., Weinrebe, G., 2005. Design of commercial solar updraft tower systems – utilization of solar induced convective flows for power generation. J. Sol. Energy Eng. 127, 117–124.

Seaton, A., MacNee, W., Donaldson, K., Godden, D., 1995. Particulate air pollution and acute health effects. Lancet 345, 176–178.

Seinfeld, J.H., Pandis, S.N., 2006. Atmospheric Chemistry and Physics – From Air Pollution to Climate Change. Second Edition. Wiley-Interscience, Hoboken, NJ.

Shah, A.S.V., Langrish, J.P., Nair, H., McAllister, D.A., Hunter, A.L., Donaldson, K., Newby, D.E., Mills, N.L., 2013. Global association of air pollution and heart failure: a systematic review and meta-analysis. Lancet 382, 1039–1048.

Shi, H., Wang, Y., Chen, J., Huisingh, D., 2016. Preventing smog crises in China and globally. J. Clean. Prod. 112, 1261–1271.

Skamarock, W.C., Klemp, J.B., 2008. A time-split nonhydrostatic atmospheric model for weather research and forecasting applications. J. Comput. Phys. 227, 3465–3485.

Skamarock, W.C., Klemp, J.B., Dudhia, J., Gill, D.O., Barker, D.M., Duda, M.G., Huang, X.-Y., Wang, W., Powers, J.G., A Description of the Advanced Research WRF Version 3. NCAR Tech. Note NCAR/TN-468+STR (113 pp).

Sun, Y., Du, W., Fu, P., Wang, Q., Li, J., Ge, X., Zhang, Q., Zhu, C., Ren, L., Xu, W., Zhao, J., Han, T., Worsnop, D.R., Wang, Z., 2016. Primary and second aerosols in Beijing in winter: sources, variations and processes. Atmos. Chem. Phys. 16, 8309–8329.

Tang, G., Zhao, P., Wang, Y., Gao, W., Cheng, M., Xin, J., Li, X., Wang, Y., 2017. Mortality and air pollution in Beijing: the long-term relationship. Atmos. Environ. 150, 238–243.

The NCAR Command Language (Version 6.4.0) (Software), 2017. Boulder, Colorado: UCAR/NCAR/CISL/TDD. https://doi.org/10.5065/D6WD3XH5.

Wang, H., Skamarock, W.C., Feingold, G., 2009. Evaluation of scalar advection schemes in the advanced research WRF model using large-eddy simulations of aerosol-cloud interactions. Mon. Weather Rev. 137, 2547–2558.

Wang, H., Zhao, L., Xie, Y., Hu, Q., 2016a. "APEC blue" – the effects and implications of joint pollution prevention and control program. Sci. Total Environ. 553, 429–438.

Wang, Y., Zhang, Y., Schauer, J.J., de Foy, B., Guo, B., Zhang, Y., 2016b. Relative impact of emissions controls and meteorology on air pollution mitigation associated with the Asia-Pacific Economic Cooperation (APEC) conference in Beijing, China. Sci. Total Environ. 571, 1467–1476.

Wang, Y., Xue, Y., Tian, H., Gao, J., Chen, Y., Zhu, C., Liu, H., Wang, K., Hua, S., Liu, S., Shao, P., 2017. Effectiveness of temporary control measures for lowering PM$_{2.5}$ pollution in Beijing and the implications. Atmos. Environ. 157, 75–83.

Wicker, L.J., Skamarock, W.C., 2002. Time-splitting methods for elastic models using forward time schemes. Mon. Weather Rev. 130, 2088–2097.

Zhang, H., Wang, S., Hao, J., Wang, X., Wang, S., Chai, F., Li, M., 2016. Air pollution and control action in Beijing. J. Clean. Prod. 112, 1519–1527.